nature communications

Article

https://doi.org/10.1038/s41467-025-60151-3

Interface engineering to regulate oxidation dynamics of supported nanoparticles

Received: 18 November 2024

Accepted: 14 May 2025

Published online: 24 May 2025

Check for updates

Shiyuan Chen[1,3], Kai Zhang[1,3], Yuhui Chen[1], Bo Shao[1], Chaobin Zeng[2], Wentao Yuan[1], Hangsheng Yang[1], Zhong-Kang Han[1] ✉, Ying Jiang[1] ✉, Ze Zhang[1] & Yong Wang[1] ✉

Understanding the oxidation of metal nanoparticles is crucial for various applications, particularly in heterogeneous catalysis, such as catalytic oxidation reactions, where metal nanoparticles are typically dispersed on supports. However, the dynamics of interaction between nanoparticles and oxygen, especially under the influence of supporting materials, remain poorly understood, significantly hindering the precise comprehension and regulation of nanoparticle oxidation dynamics. Here, we elucidate two distinct oxidation dynamics in supported nanoparticles using aberration-corrected environmental (scanning) transmission electron microscopy (E(S)TEM), i.e., preferential self-adaptive oxidation initiating at the nanoparticle-support interface, where the support facilitates oxidation, and surface oxidation, where the support inhibits oxidation. Our systematic calculations, corroborated by experimental validations, demonstrate that the interfacial epitaxial match plays a dominant role in determining the oxidation dynamics in oxygen. It serves as a key indicator for developing a straightforward interface engineering strategy to regulate both self-adaptive and surface oxidation processes. This work highlights the diversity of interface-determined oxidation behaviors and offers a strategy for regulating the oxidation dynamics of supported nanoparticles under identical conditions.

Many nanomaterials undergo oxidation under industrially and environmentally relevant conditions[1–3]. Their unique characteristics, such as the small sizes, diverse morphologies, abundant surface defects, and complex interfacial structures, lead to distinct oxidation behaviors compared to the bulk counterparts, often resulting in different structural evolution and altered reactivity[4–10]. Prior investigations have elucidated critical structural factors in the oxide formation and growth, including twining, strain and mismatch dislocation movement[1,11,12]. Nevertheless, for supported nanoparticles that are renowned in heterogeneous catalysis, situations become more intricate, due to the additional influence of metal-support interfaces, alongside metal-oxygen interactions[13]. Therefore, in addition to the structural characteristics of the metal nanoparticles themselves, attention should also be paid to the support influence on the oxidation behavior of supported nanoparticles.

It has been reported that the oxygen storage capacity of the supports influences the oxidation of supported nanoparticles[14–18]. Farrauto et al.[16] and Nilsson et al.[17] demonstrated that reducible CeO_2 supports could promote the formation and stability of supported metal oxides, compared with other inactive supports like Ta_2O_3, Al_2O_3, and ZrO_2. Regarding the oxidation dynamics, unlike free nanoparticles where oxidation always nucleates on the metal surface, supported nanoparticles can have a greater diversity of oxide species, making the oxidation process more complex and less predictable[19–21]. For

[1]Center of Electron Microscopy and State Key Laboratory of Silicon and Advanced Semiconductor Materials, School of Materials Science and Engineering, Zhejiang University, Hangzhou, China. [2]Hitachi High-Technologies (Shanghai) Co., Ltd., Shanghai, China. [3]These authors contributed equally: Shiyuan Chen, Kai Zhang. ✉e-mail: hanzk@zju.edu.cn; yjiang0209@zju.edu.cn; yongwang@zju.edu.cn

example, Schalow et al.[22] studied the oxide species in Pd/Fe_3O_4 during CO oxidation, and manifested the preferential formation of an interface oxide layer, which is stabilized by the metal-support interaction. Such interfacial oxidation dynamics could modulate the CO oxidation pathway by creating an oxygen reservoir that enables the reversible storage and release of oxygen during the catalytic process. Currently, the specific effects of supports on oxidation dynamics have yet to be fully elucidated. In particular, the question remains as to how metal-support interfaces influence and regulate the metal oxidation dynamics and interfacial atomic configurations, which are crucial for understanding and optimizing the catalytic performance.

Here, utilizing aberration-corrected E(S)TEM techniques in couple with well-defined Pd/CeO_2 models, we provide atomic-scale, in situ experimental evidence of two distinct oxidation dynamics. When supported on CeO_2(100), Pd nanoparticles undergo self-adaptive oxidation, facilitating the dominant formation of interface oxides, the structure of which is independent of the internal defects in Pd nanoparticles and initial crystallographic relationships between Pd and CeO_2. In contrast, Pd nanoparticles on CeO_2(111) exhibit a higher surface oxidation reactivity. A simple epitaxial matching rule enables the regulation of both self-adaptive and surface oxidation processes through interface engineering. Utilizing this strategy, we identify a self-adaptive oxidation system in Ni/MgO, whose support is non-reducible and has nearly no lattice mismatch with the formed interface oxide. Additionally, the predicted preferential surface oxidation of Ru/CeO_2(100) further confirms the effectiveness of this strategy. This work challenges the views that primarily attribute enhanced interfacial oxidation to strain effects and the reducibility of the support, introducing an approach for tailoring the oxidation dynamics of supported nanoparticles by manipulating the facet-dependent interface epitaxy.

Results and discussion

In this study, CeO_2 supports were hydrothermally synthesized and subsequently loaded with Pd nanoparticles using a solid grinding method. The Pd loading level was determined to be approximately 1.3 wt% through inductively coupled plasma atomic emission spectroscopy (ICP-AES). A typical low-magnification high-angle annular dark-field STEM (HAADF-STEM) image (illustrated in Supplementary Fig. 1a) reveals the uniform morphology of CeO_2 nanocubes, which range in size from 20 to 100 nm. As shown in Supplementary Fig. 1b, c, the atom-resolved HAADF-STEM images clearly show clean surfaces and an interplanar spacing of 0.271 nm along the [001] zone axis, confirming the termination of {100} facets for the CeO_2 nanocubes. The Pd nanoparticles are homogeneously dispersed on the CeO_2(100) surfaces, with an average size of approximately 4.5 nm (ranging from 2 to 7 nm). The lattice spacings of 0.224 and 0.194 nm match well with the interplanar spacings of Pd(111) and Pd(200) facets (Supplementary Table 1), respectively.

To remove any possible oxide species from the Pd nanoparticles, the as-prepared Pd/CeO_2(100) nanoparticles were pretreated in H_2 (50 mL min^{-1}) at 300 °C for 3 h in a tube furnace (Hefei Kejing OTF-1200X). As shown in Fig. 1a, the HAADF-ESTEM image indicates that the reduced Pd nanoparticle supported on CeO_2(100) exhibits homogeneous contrast throughout the entire particle, indicating effective reduction. Twinning may occasionally occur within the nanoparticles as a result of the grinding process. Subsequent oxidation experiments were carried out on a Cs-corrected ESTEM (Hitachi HF5000). Initially, oxygen was introduced to create an atmosphere with a pressure of 5 Pa, followed by a temperature increase to 350 °C. Exposing the Pd/CeO_2(100) nanoparticles to such oxidizing conditions for 8 min leads to observable slight contrast variations at the corner of interface between Pd nanoparticle and CeO_2(100), as marked by red arrows in Fig. 1b. This change is critical evidence of oxidation, as lattice expansion in three dimensions, accompanied by the incorporation of the lighter element oxygen, causes a decrease in electron scattering intensity per unit area, resulting in darker regions in HAADF-ESTEM images. Therefore, the darker areas of each particle represent the oxidized Pd phase, while the brighter areas remain metallic Pd. This initial contrast decrease at the interface corner indicates that oxidation preferentially nucleates at the metal-support-oxygen interface (i.e., Pd/CeO_2(100) interface) rather than the single metal-oxygen interface (i.e., the free surface of Pd) or the twin boundary[23], highlighting the

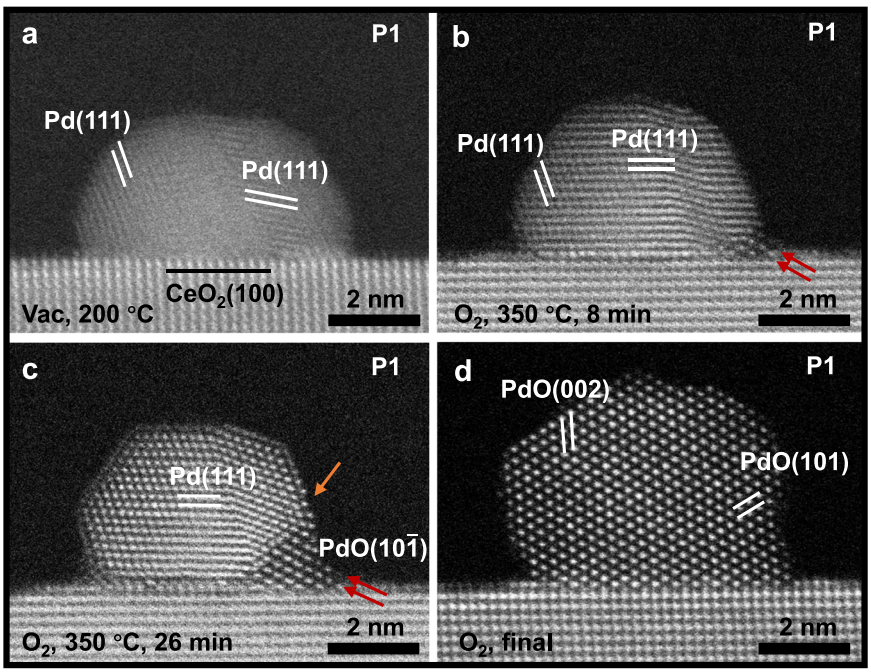

Fig. 1 | In situ oxidation of Pd/CeO_2(100) in 5 Pa oxygen at 350 °C. a–c Time-sequenced HAADF-ESTEM (high-angle annular dark field-environmental scanning transmission electron microscopy) images depicting the formation of PdO for a specific nanoparticle, labeled as P1 (red arrows: interface oxide species; orange arrow: surface oxide layer). **d** Final state of the oxidized nanoparticle.

https://doi.org/10.1038/s41467-025-60151-3

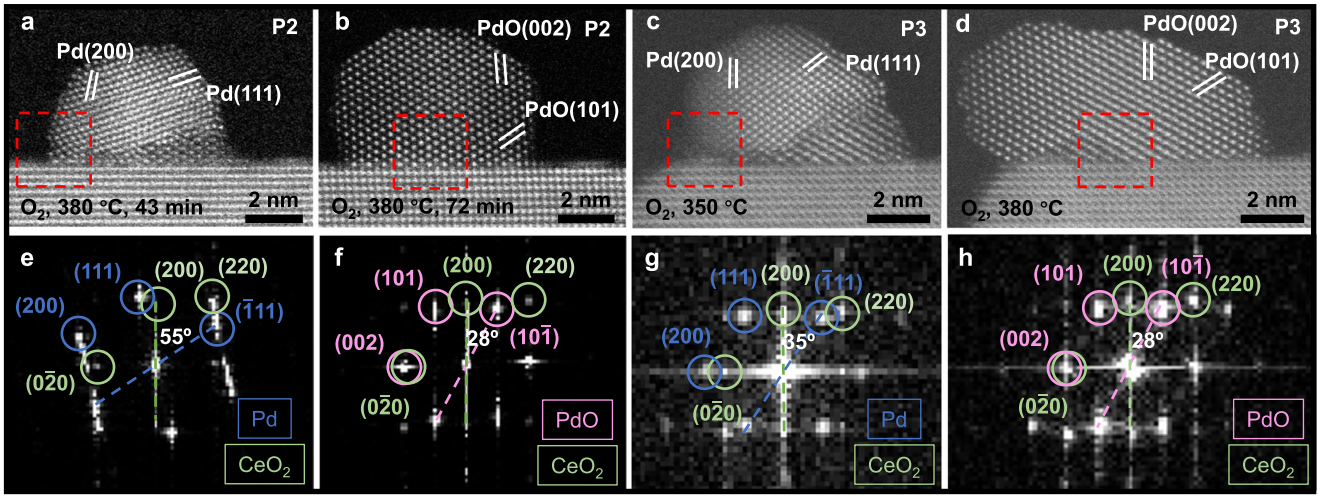

Fig. 2 | Crystallographic relationships between Pd, PdO and CeO_2. **a**–**d** HAADF-ESTEM (high-angle annular dark field-environmental scanning transmission electron microscopy) images of the intermediate and final states during the oxidation of the second nanoparticle (P2, **a**, **b**) and third nanoparticle (P3, **c**, **d**). **e**–**h** FFT (fast Fourier transform) patterns obtained from the dashed red squares in (**a**–**d**) showing the rotation angles between the Pd($\bar{1}11$) and CeO_2(200), as well as PdO($10\bar{1}$) and CeO_2(200) reflections. Blue circles correspond to the Pd patterns, pink to the PdO patterns, and green to the CeO_2 patterns.

interface's unique role in oxidation processes. Specifically, the oxidation tends to nucleate at the corners formed between Pd{111} and CeO_2{100}, since the remaining metallic Pd preferentially exposes the {111} facets at the Pd-PdO interface due to their closest atomic packing and low surface energy.

Maintaining the same reaction conditions for 26 min (Fig. 1c), the atomic d-spacing of the outermost surface layer expands (indicated by an orange arrow), signifying the formation of a surface oxide layer. Notably, over time, this oxide formation remains confined to the outermost surface layer, with no inward progression observed[24]. Conversely, the interface oxide species at the Pd-CeO_2(100) interface tend to develop towards the upper part of the nanoparticle. Remarkably, it subsequently takes less than 1 min for the interface oxide to traverse the entire particle and complete the oxidation process. Comparing the two potential oxidation pathways, i.e., oxidation from the free surface and oxidation from the confined interface, it becomes clear that the latter exhibits faster nucleation and growth of oxides, thus accelerating the oxidation process.

Figure 1d reveals the final state of the oxidized nanoparticle. The lattice spacings measured at 0.265 and 0.263 nm correspond to the interplanar spacings of the PdO(002) and PdO(101) facets (Supplementary Table 1), respectively, which are the terminations of the faceted PdO nanoparticle. Despite the presence of a twin boundary in the initial Pd nanoparticle, no such defect was observed in the newly formed PdO nanoparticle. These observations suggest that the microstructure of Pd has a neglected effect on the formation and microstructure of PdO. It is also important to note that the sequential images were acquired at regular intervals of a few minutes, and the electron beam was blanked between exposures to eliminate the potential beam effects on the observations.

Oxidation behaviors of two additional Pd nanoparticles with distinct orientations on CeO_2(100) supports were shown in Fig. 2a–d, with further information available in Supplementary Figs. 2 and 3. For clarity, the Pd nanoparticle shown in Fig. 1 is labeled as P1, the nanoparticle in Fig. 2a, b as P2, and the nanoparticle in Fig. 2c, d as P3. Similar to P1, the nucleation and growth of interface oxides on P2 and P3 occur more readily than those of the surface oxides, with the oxidation of Pd nanoparticles progressing away from the interface. Previous studies on the oxidation of single-crystal metal nanoparticles have shown that the oxidized phase typically grows epitaxially on the metal nanoparticles[9,25,26], and it was believed that the structure of the oxidized phase would be affected by this epitaxial growth. However, in our supported nanoparticle systems, the relationship between Pd and PdO is not fixed, as shown in Supplementary Fig. 4, indicating that the oxidation is predominantly governed by the Pd-CeO_2(100) interface. This also leads to atomic disorders at the Pd-PdO interface during the mass transport process during oxidation.

As shown in Supplementary Fig. 5 and Fig. 2, the HAADF-ESTEM images and corresponding fast Fourier transform (FFT) patterns demonstrate that the orientation relationship between the as-prepared Pd nanoparticles and CeO_2 varies, with the angles between Pd($\bar{1}11$) and CeO_2(200) measured at ~0°, 55°, and 35° for P1, P2, and P3, respectively. In contrast, the newly formed PdO nanoparticles exhibit a consistent epitaxial relationship with CeO_2(200), consistently forming an angle of 28° between PdO($10\bar{1}$) and CeO_2(200), although lattice distortions may arise due to the confinement of Pd nanoparticles and CeO_2 supports when the PdO layer is thin. This epitaxial relationship indicates that PdO and CeO_2(100) match well, with continuous Ce and Pd lattice sites across the interface. According to the FFT patterns, the epitaxial relationship can be determined as PdO(002) parallel to CeO_2(010), and PdO[010] parallel to CeO_2[001]. This epitaxy and coherent interface suggest a low interface energy, which not only facilitates rapid nucleation but also stabilizes the oxides at the interface[27]. To show the epitaxy between PdO and CeO_2 more clearly, we captured the in situ oxidation process of Pd/CeO_2{100} from a top-down view as well, as shown in Supplementary Fig. 6a–c. After oxidation, the PdO forms a faceted morphology and exhibits a good epitaxial relationship with the underlying CeO_2 (PdO(002)//CeO_2(010) and PdO[010]//CeO_2[001]), consistent with our inference from the side-view analysis. Furthermore, the models of PdO, CeO_2, and a 2D atomic visualization of the PdO-CeO_2 interface were presented to enhance the understanding of their relationship, as illustrated in Supplementary Fig. 6d–f.

As is known, CeO_2 is a reducible support and may enhance the Pd oxidation[16,17]. To further assess the influence of interface structure in addition to the support composition on oxidation dynamics, we investigated the oxidation of Pd nanoparticles supported on CeO_2(111). The Pd nanoparticles were loaded on CeO_2 nanooctahedra in the same way as Pd/CeO_2(100), predominantly forming clean Pd-CeO_2(111) interfaces, as shown in Supplementary Fig. 1d–f. In order to obtain the continuous dynamics of the oxidation process and further mitigate the impact of the electron beam, oxidation experiments were performed

https://doi.org/10.1038/s41467-025-60151-3

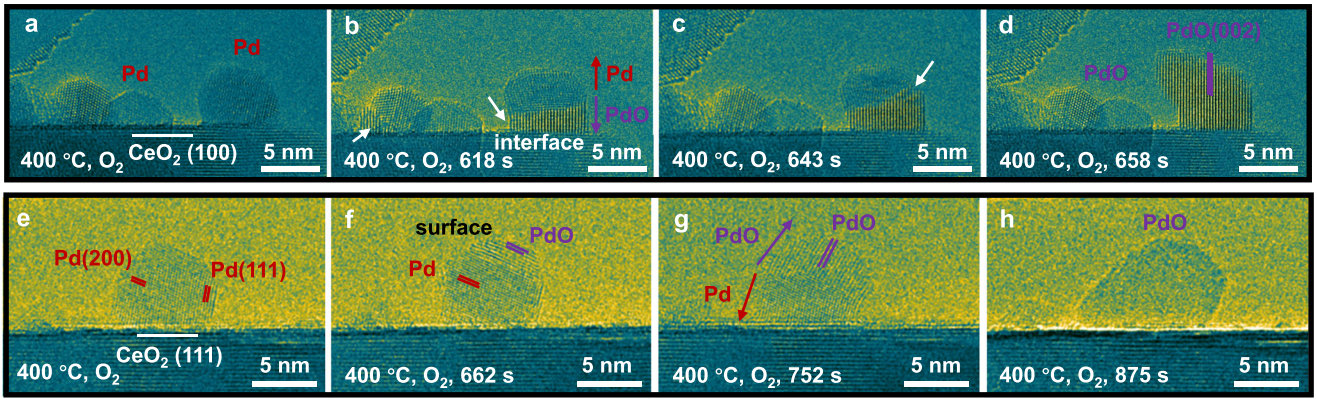

Fig. 3 | Sequential in situ ETEM (environmental transmission electron microscopy) images showing the oxidation processes of Pd/CeO_2 nanoparticles in 5 Pa O_2 at 400 °C. In situ HRTEM (high resolution transmission electron microscopy) images of **a**–**d** Pd/CeO_2(100) (white arrows: interface oxide species) and **e**–**h** Pd/CeO_2(111) nanoparticles.

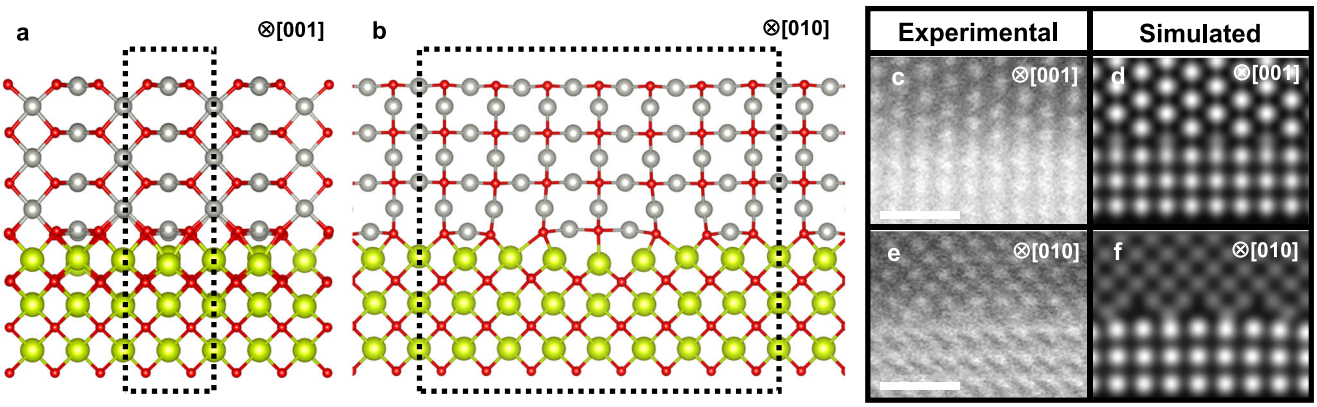

Fig. 4 | The structure of PdO(100)/CeO_2(100) heterojunction and comparison between experimental and simulated HAADF-STEM (high-angle annular dark field-scanning transmission electron microscopy) images. a, **b** Constructed PdO(100)/CeO_2(100) heterojunction structure along zone axis of CeO_2[001] and CeO_2[010], respectively (gray balls: Pd atoms; yellow green balls: Ce atoms; red balls: O atoms; dashed-line wireframe: crystal periodicity). **c**–**f** Experimental and simulated HAADF-STEM image of structure along zone axis of CeO_2 [001] and CeO_2 [010] (scale bar: 1 nm).

within a Cs-corrected ETEM (FEI Titan 80-300 ST) at 400 °C in a 5 Pa oxygen atmosphere along with a Gatan OneView complementary metal-oxide semiconductor camera to capture the atomic images of the intrinsic particle/interface structure in a lower beam dose mode (1×10^3 to 3×10^3 e/Å^2 s). In situ high-resolution TEM (HRTEM) images presented in Fig. 3a–d illustrate the Pd nanoparticles supported on the CeO_2(100) surface, and Fig. 3e–h shows sequential images for the Pd/CeO_2(111) nanoparticles. Similar to observations in ESTEM (Fig. 1), PdO nucleation at the Pd-CeO_2(100) interface spreads across the particle, resulting in a single PdO phase that exhibits an epitaxial relationship of PdO(002)//CeO_2(010) and PdO[010]//CeO_2[001] (Supplementary Movie 1). Conversely, for the Pd/CeO_2(111) nanoparticles, oxidation begins at the surface and is predominantly characterized by the subsequent growth of surface oxides. The completion of oxidation at the Pd-CeO_2(111) interface suggests that the Pd-CeO_2(111) interface blocks the oxidation, with Pd atoms near the interface tending to maintain their metallic state (Supplementary Movie 2). Additionally, as anticipated, no epitaxial relationship was observed between PdO and CeO_2(111). Therefore, in comparison to the Pd-CeO_2(100) interface, the Pd-CeO_2(111) interface does not promote oxidation; instead, it inhibits the interaction between Pd and the reactive oxygen.

The oxidation in Pd/CeO_2(100) is defined as self-adaptive oxidation, characterized by interfacial oxidation to form the stable alignment between the metal oxide and support, elimination of native defects (e.g., twinning) in metal nanoparticles, and random orientations between metal and metal oxide during oxidation. The behavior underscores the critical influence of interface structures on the dynamics of self-adaptive oxidation. To investigate the formation mechanisms of interfacial Pd oxides and the enhanced oxidation at these interfaces, systematic density functional theory (DFT) calculations were performed. Guided by experimental HAADF-STEM images (Figs. 1 and 2 and Supplementary Fig. 6a–c) of the PdO(100)/CeO_2(100) heterojunction along both the [001] and [010] zone axes of CeO_2, we constructed a heterojunction model (shown in Supplementary Data 1) comprising a PdO(100) slab with a (1 × 7) supercell (PdO: a = b = 3.09 Å, c = 5.41 Å, α = β = γ = 90°, shown in Supplementary Fig. 6d) and a CeO_2(100) slab with a (1 × 4) supercell (CeO_2: a = b = c = 5.49 Å, α = β = γ = 90°, shown in Supplementary Fig. 6e). The constructed model (Fig. 4a, b) exhibits negligible lattice mismatch along both the [001] and [010] zone axes of CeO_2. To obtain the detailed atomic structure of the interface, we employed a differential evolution algorithm (DEA), as implemented in the IM^{2}ODE package, to globally search for interface structures with varying compositional ratios by modulating the number of interfacial oxygen atoms. By optimizing over 500 structures via the DEA global search process, we identified a stable structural model that is consistent with the experimental observations (Supplementary Fig. 6 and Fig. 4c–f). The accuracy of the model was confirmed by simulating HAADF-STEM images along two

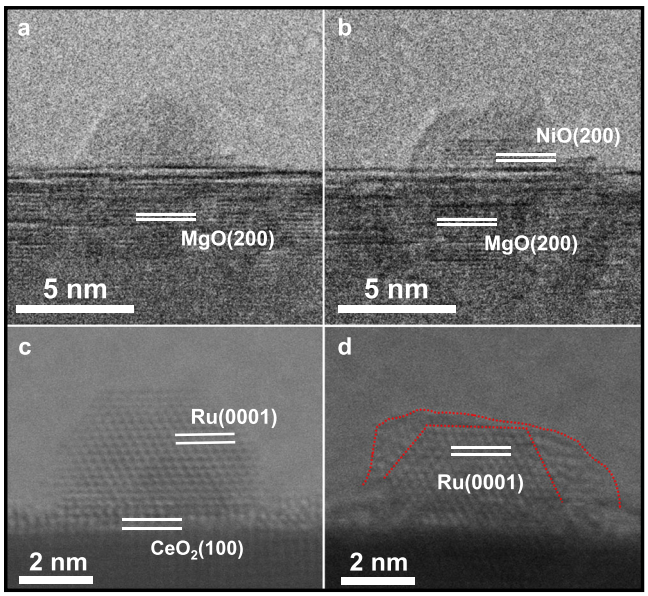

Fig. 5 | Self-adaptive oxidation in Ni/MgO(100) and surface oxidation in Ru/CeO_2(100). a, **b** In situ oxidation of Ni/MgO(100) (**a** vacuum; **b** 4.5×10^{-2} Pa O_2, 300 °C). **c**, **d** In situ oxidation of Ru/CeO_2(100) (**c** vacuum; **d** 3 Pa O_2, 200 °C; red dashed line: oxidized Ru zone).

zone axes and comparing them with the corresponding experimental data (Fig. 4c–f). The column positions and contrasts in the simulated images closely match those in the experimental images. The calculated interface energy of the heterojunction is −0.24 eV/Å^2, indicating its high stability.

In contrast, in the Pd/CeO_2(111) system, no effective epitaxial relationship exists between CeO_2(111) and any low-index facets of PdO due to high lattice mismatches (Supplementary Table 2). The interfacial epitaxial mismatches in the Pd/CeO_2(111) system are significantly larger than those in the Pd/CeO_2(100) system, which is insufficient to facilitate interfacial oxidation in the Pd/CeO_2(111) system. These results indicate that the interfacial epitaxial match plays a dominant role in determining the distinct oxidation dynamics, and a small mismatch favors self-adaptative oxidation at the interface, while a large mismatch results in higher surface oxidation reactivity. Consequently, we propose an interface engineering strategy that uses the interfacial epitaxial match as an indicator to regulate the oxidation reactivity of supported nanoparticles. By selecting support facets that create a small interfacial epitaxial mismatch, nanoparticles preferentially oxidize at the interface, forming oxides with fixed epitaxial relationships regardless of internal metal defects or the initial crystallographic relationship between the metal and the support. This ensures that the interface oxide forms a thermodynamically stable and adaptive bond with the support. Conversely, choosing support facets that do not yield a small interfacial epitaxial mismatch with the common surface cuts of the supported metal oxides allows for oxidation processes that begin at the surface, thereby tailoring the oxidation pathway to meet specific requirements.

To validate the effectiveness of this strategy, we analyzed the interfacial epitaxial match in other systems (Supplementary Table 2), specifically Ni/MgO(100) and Ru/CeO_2(100). MgO, a non-reducible support, shares a similar crystalline structure with NiO and has closely matched lattice constants (a(NiO) = 4.186 Å and a(MgO) = 4.194 Å, resulting in a mismatch of less than 0.2%) (Supplementary Table 2). Conversely, RuO_2 (a = 6.335 Å, c = 3.11 Å) lacks a clear epitaxial relationship with CeO_2(100) (d = 2.7 Å) (Supplementary Table 2). As shown in Fig. 5a, b, NiO forms at the Ni-MgO interface in a self-adaptive manner (NiO(100)//MgO(100)), rather than on the free surface, despite Ni's high susceptibility to oxidation. This confirms that the interface engineering strategy is effective even with non-reducible oxide supports and in systems where the interfacial strain between the oxides is minimal. Conversely, in situ experiments as displayed in Fig. 5c, d show that oxidation predominantly occurs on the free surface of Ru nanoparticles, not at the Ru-CeO_2(100) interface, similar to the behavior observed in the Pd/CeO_2(111) system. These experimental results indicate that the support reducibility is not the decisive factor in surface or interface oxidation dynamics, and validate the effectiveness of interface engineering strategy that uses the interfacial epitaxial match as an indicator to regulate the oxidation reactivity of supported nanoparticles.

In conclusion, our findings reveal an interface engineering strategy for regulating the oxidation dynamics of supported nanoparticles in oxygen by combining atom-resolved Cs-corrected E(S)TEM techniques with a differential evolution algorithm. We found that the interfacial epitaxial match plays a critical role in determining whether oxidation occurs as surface oxidation or in a self-adaptive oxidation manner. In systems with good epitaxial matching, typically with mismatches within 5%, oxidation tends to proceed in a self-adaptive manner, facilitating the formation of epitaxial interface oxides regardless of the historical configurations of the metal nanoparticles. Conversely, in systems with poor epitaxial matching, surface oxides form instead, and metal atoms near the interface are more likely to remain in the metallic state. The effectiveness of this strategy was experimentally validated across the Pd/CeO_2, Ni/MgO, and Ru/CeO_2 systems, irrespective of the support's reducibility or interfacial strain. Our findings not only provide clear atomic-scale observations and theoretical insights into the effects of support on nanoparticle oxidation but also open avenues for customizing oxidation dynamics to enhance materials' performance.

Methods

Preparations of Pd/CeO_2(100) and Pd/CeO_2(111)

CeO_2(100) nanocubes were hydrothermally prepared by dissolving 38.4 g NaOH and 3.472 g $Ce(NO)_3{\cdot}6H_2O$ in 140 and 20 mL deionized water, respectively[28]. Then $Ce(NO_3)_3$ solution was dropped into the NaOH solution, with the mixed solution being stirred continuously at ambient temperature for 30 min and transferred into a Teflon-lined stainless-steel autoclave and hydrothermally treated at 180 °C for 24 h. After the hydrothermal treatment, the precipitates were washed with deionized water and separated by centrifugation repeatedly, then dried overnight at 80 °C and pretreated in the air at 600 °C for 2 h.

For CeO_2(111), 0.0152 g Na_3PO_4 and 1.716 g $Ce(NO)_3{\cdot}6H_2O$ were dissolved in 140 and 20 mL deionized water, respectively[29]. Then $Ce(NO_3)_3$ solution was dropped into the Na_3PO_4 solution and stirred continuously at ambient temperature for 30 min, and then the mixed solution was poured into a Teflon-lined stainless-steel autoclave and hydrothermally treated at 170 °C for 12 h. After the hydrothermal treatment, the precipitates were washed with deionized water and separated by centrifugation repeatedly, then dried overnight at 80 °C and pretreated in the air at 600 °C for 2 h.

Pd nanoparticles were loaded on CeO_2(100) and CeO_2(111) via the solid grinding method[30]. Specifically, $Pd(acac)_2$ powders and CeO_2 powders were mixed and milled in a mortar pestle for 30 min. Then, it was pretreated in air at 200 °C for 2 h to stabilize the Pd species and finally heated at 300 °C for 2 h under 10% H_2/Ar. The Pd loadings are approximately 1.3%, which were measured via ICP-AES (PerkinElmer NexION 300X).

Preparations of Ni/MgO(100)

MgO nanocubes with {100} surfaces were prepared by burning magnesium wires in air and collecting the combustion smoke[31]. The Ni nanoparticles were prepared according to a reported method[32]. First, 257 mg

of $Ni(acac)_2$ (1 mmol), 15 mL oleylamine (OAm) and 0.32 mL (1 mmol) oleic acid (OA) were mixed together under a nitrogen flow. The mixed solution was heated to 110 °C in 20 min until it turned green. The solution was then kept at 110 °C for 1 h. Later, the solution was cooled down to 90 °C, and then 64 mg of borane tributylamine (BTB) (solvated in 2 mL of OAm) was quickly injected. The color of the solution was observed to change from green to dark brown. After the reaction, the solution was cooled down to room temperature, and the Ni nanoparticles were separated by centrifugation (8000×*g* for 8 min) after adding 30 mL of ethanol. Finally, Ni nanoparticles were dispersed in toluene. Ni/MgO(100) nanoparticles were prepared through the impregnation method. The nominal Ni content is 1.5 wt %. First, a certain amount of Ni nanoparticles was dissolved in toluene, and the MgO nanocubes were then added to the solution. Later, the mixed solution was dispersed by ultrasonic dispersion at room temperature until the toluene was completely evaporated. Finally, the white powder left by the evaporation of toluene was collected as the Ni/MgO(100) nanoparticles.

Preparation of $Ru/CeO_2(100)$

$Ru/CeO_2(100)$ nanoparticles were prepared through the impregnation method[33]. First, $Ru(NO)(NO_3)_3$ was dissolved in deionized water, and the CeO_2 nanocubes were then added to the solution. Later, the mixed solution was dispersed by ultrasonic dispersion at room temperature and then stirred at 90 °C until the water was completely evaporated. Finally, the yellow powder was reduced in hydrogen with a flow rate of 50 mL/min at 500 °C for 3 h and was herein denoted as $Ru/CeO_2(100)$ nanoparticles.

In situ ESTEM characterizations of Pd/CeO_2 and Ru/CeO_2

The in situ ESTEM experiments were performed in a HITACHI HF5000, 200 kV aberration-corrected TEM/STEM, with gas environment (10^{-5} Pa to 10 Pa) available. The instrument is equipped with an annular dark-field STEM (DF-STEM) detector. The $Pd/CeO_2(100)$ nanoparticles and $Ru/CeO_2(100)$ nanoparticles were first dispersed on a heating chip, and then loaded into the ESTEM through a single-tilt heating holder (a MEMS holder). In addition, to observe the oxidation information, a dark-field detector was used to record the images. The nanoparticles were exposed to the beam only during data setup and acquisition, with each image frame captured over a 20-s exposure. The images have 1024 × 1024 pixels, with a pixel dwell time of 19.07 µs. The convergence and collection angles were respectively ~23 mrad and 40–213 mrad (half angle), and the probe current was ~47 pA.

In situ ETEM characterizations of Pd/CeO_2

The in situ TEM experiments were performed in a spherical aberration-corrected ETEM (FEI Titan 80-300 ST), with gas environment (10^{-7} mbar to 10 mbar) available. The ETEM was operated at 300 kV, which could provide an information resolution of ~0.08 nm. The Pd/CeO_2 nanoparticles in ethanol solution were first dispersed on a SiN_x-based heating chip, and then loaded into the ETEM by a single-tilt heating holder (Wildfire S3, DENS solutions). A Gatan Oneview camera system was used to record the dynamic behaviors of Pd/CeO_2 nanoparticles. Images were recorded with a time resolution of 0.5 s per 4096 × 4096 frame.

In situ ETEM characterizations of Ni/MgO

The ETEM experiments were performed in a Hitachi H-9500 ETEM (300 kV), with a spatial resolution of 2 Å. A chipnova double tilt heating holder (CNT-SHBO-D) is used in our experiments. The prepared Ni/MgO nanoparticles were dispersed on chips and then loaded into the microscope through the heating holder. In a typical in situ heating experiment, the Ni/MgO nanoparticles were captured in vacuum (10^{-4} Pa) and at room temperature first. Then the Ni/MgO nanoparticles were heated to 300 °C with a heating rate of 5 °C s^{-1}, followed by the introduction of oxygen (0.045 Pa).

Computational details

We used DFT with projected augmented wave (PAW) potentials implemented in the Vienna ab initio simulation package (VASP) for our theoretical calculations[34,35]. The generalized gradient approximation (GGA) with the Perdew-Burke-Ernzerhof (PBE) functional was employed to describe the exchange correlation effects[36]. A plane-wave cutoff energy of 400 eV was used[37]. During structural optimization, the convergence criteria for the forces and total energy were set to 0.05 eV/Å and 10^{-4} eV, respectively. For systems containing CeO_2, the DFT + U method (U = 5.0 eV)[38] was applied to correct for self-interaction errors. A 1 × 1 × 1 gamma-centered *k*-point mesh was used for the PdO-CeO_2 heterojunction structure. For the PdO(100)//CeO_2(100) heterojunction model, the PdO(100)-(1 × 7) surface structure (Fig. 4a, b) consists of 3 layers of Pd atoms and 4 layers of Pd-O atoms, while the CeO_2(100)-c(1 × 4) surface structure consists 3 layers of Ce atoms, 3 layers of O atoms. To simulate bulk CeO_2 conditions, the bottom three layers of the ceria slab are fixed. We conducted a structural search (Supplementary Fig. 7) using the IM^2ODE program[39,40]. The computational cell includes a layer spanning a 4 Å height range, from the top Ce layer to the bottom Pd-O layer, where we introduced x Pd atoms (x = 10, 11, 12) along with y O atoms (y = 13, 14, 15) onto the top Ce layer, as shown in Supplementary Fig. 7. We set the minimum bond lengths for the generated structures as follows: Ce-Ce, 3.5 Å; Ce-O, 2.1 Å; Ce-Pd, 2.5 Å; Pd-O, 1.8 Å; Pd-Pd, 2.9 Å; and O-O, 2.4 Å. The structural search followed an iterative process, with each new generation of structures derived from the most stable configurations of the previous generation. For each Pd/O ratio, we explored approximately 100 structures across 10 DE generations, with each generation containing around 10 structures. The DE ratio, which determines the ratio of structures generated by the DE algorithm and random structures, was set to 0.6. The relative energies, computed via DFT, were then ranked from lowest to highest.

Data availability

The data that support the findings of this study are available from the corresponding authors upon request due to the ongoing study.

References

1. Pratt, A. et al. Enhanced oxidation of nanoparticles through strain-mediated ionic transport. *Nat. Mater.* **13**, 26–30 (2014).
2. Nair, S. et al. Engineering metal oxidation using epitaxial strain. *Nat. Nanotechnol.* **18**, 1005–1011 (2023).
3. Liu, X. et al. Atomically resolved transition pathways of iron redox. *J. Am. Chem. Soc.* **146**, 17487–17494 (2024).
4. You, R. et al. Revealing temperature-dependent oxidation dynamics of Ni nanoparticles via ambient pressure transmission electron microscopy. *Nano Lett.* **23**, 7260–7266 (2023).
5. Anderson, B. & Tracy, J. Nanoparticle conversion chemistry: Kirkendall effect, galvanic exchange, and anion exchange. *Nanoscale* **6**, 12195–12216 (2014).
6. Fu, Q. et al. Interface-confined ferrous centers for catalytic oxidation. *Science* **328**, 1141–1144 (2010).
7. Huang, C., Weng, W., Liao, C. & Tu, K. Suppression of interdiffusion-induced voiding in oxidation of copper nanowires with twin-modified surface. *Nat. Commun.* **9**, 340 (2018).
8. Huang, X. et al. Phase coexistence and structural dynamics of redox metal catalysts revealed by operando TEM. *Adv. Mater.* **33**, 2101772 (2021).
9. LaGrow, A. P., Ward, M. R., Lloyd, D. C., Gai, P. L. & Boyes, E. D. Visualizing the Cu/Cu_2O interface transition in nanoparticles with environmental scanning transmission electron microscopy. *J. Am. Chem. Soc.* **139**, 179–185 (2017).
10. Ou, Y., Li, S., Yuan, W., Zhang, Z. & Wang, Y. Recent progress on studying the oxidation of metal nanoparticles via in situ

transmission electron microscopy: a review. *J. Chin. Electron Microsc. Soc.* **40**, 623–634 (2021).
11. Zhu, Q. et al. Defect-driven selective metal oxidation at atomic scale. *Nat. Commun.* **12**, 558 (2021).
12. Sun, X. H. et al. Dislocation-induced stop-and-go kinetics of interfacial transformations. *Nature* **607**, 708–713 (2022).
13. Jiang, D. et al. Dynamic and reversible transformations of subnanometre-sized palladium on ceria for efficient methane removal. *Nat. Catal.* **6**, 618–627 (2023).
14. Yang, L., Kresnawahjuesa, O. & Gorte, R. J. A calorimetric study of oxygen-storage in Pd/ceria and Pd/ceria-zirconia catalysts. *Catal. Lett.* **72**, 33–37 (2001).
15. Senftle, T. P., van Duin, A. C. T. & Janik, M. J. Methane activation at the Pd/CeO_2 interface. *ACS Catal.* **7**, 327–332 (2017).
16. Farrauto, R. J., Lampert, J. K., Hobson, M. C. & Waterman, E. M. Thermal-decomposition and reformation of PdO catalysts—support effects. *Appl. Catal. B Environ.* **6**, 263–270 (1995).
17. Nilsson, J. et al. Chemistry of supported palladium nanoparticles during methane oxidation. *ACS Catal.* **5**, 2481–2489 (2015).
18. Saadun, A. J. et al. Epitaxially directed iridium nanostructures on titanium dioxide for the selective hydrodechlorination of dichloromethane. *ACS Catal.* **10**, 528–542 (2020).
19. Schalow, T. et al. Size-dependent oxidation mechanism of supported Pd nanoparticles. *Angew. Chem. Int. Ed.* **45**, 3693–3697 (2006).
20. Schalow, T. et al. Oxygen-induced restructuring of a Pd/Fe_3O_4 model catalyst. *Catal. Lett.* **107**, 189–196 (2006).
21. Chen, S. Y. et al. Elucidation of active sites for CH_4 catalytic oxidation over Pd/CeO_2 via tailoring metal-support interactions. *ACS Catal.* **11**, 5666–5677 (2021).
22. Schalow, T. et al. Oxygen storage at the metal/oxide interface of catalyst nanoparticles. *Angew. Chem. Int. Ed.* **44**, 7601–7605 (2005).
23. Huang, W. X. et al. Steam-created grain boundaries for methane C-H activation in palladium catalysts. *Science* **373**, 1518–1523 (2021).
24. Burch, R. & Urbano, F. Investigation of the active state of supported palladium catalysts in the combustion of methane. *Appl. Catal. A Gen.* **124**, 121–138 (1995).
25. Yokosawa, T., Tichelaar, F. D. & Zandbergen, H. W. In-situ TEM on epitaxial and non-epitaxial oxidation of Pd and reduction of PdO at P = 0.2-0.7 bar and T = 20-650 °C. *Eur. J. Inorg. Chem.* **2016**, 3094–3102 (2016).
26. Zou, L. F., Li, J., Zakharov, D., Stach, E. A. & Zhou, G. W. In situ atomic-scale imaging of the metal/oxide interfacial transformation. *Nat. Commun.* **8**, 307 (2017).
27. Tang, X. et al. Significance of epitaxial growth of PtO_2 on rutile TiO_2 for Pt/TiO_2 catalysts. *J. Am. Chem. Soc.* **146**, 3764–3772 (2024).
28. Mai, H. X. et al. Shape-selective synthesis and oxygen storage behavior of ceria nanopolyhedra, nanorods, and nanocubes. *J. Phys. Chem. B* **109**, 24380–24385 (2005).
29. Yan, L., Yu, R. B., Chen, J. & Xing, X. R. Template-free hydrothermal synthesis of CeO_2 nano-octahedrons and nanorods: investigation of the morphology evolution. *Cryst. Growth Des.* **8**, 1474–1477 (2008).
30. Yoshida, H. et al. Temperature-dependent change in shape of platinum nanoparticles supported on CeO_2 during catalytic reactions. *Appl. Phys. Express* **4**, 3 (2011).
31. Geysermans, P., Finocchi, F., Goniakowski, J., Hacquart, R. & Jupille, J. Combination of (100), (110) and (111) facets in MgO crystals shapes from dry to wet environment. *Phys. Chem. Chem. Phys.* **11**, 2228–2233 (2009).
32. Metin, Ö, Mazumder, V., Özkar, S. & Sun, S. S. Monodisperse nickel nanoparticles and their catalysis in hydrolytic dehydrogenation of ammonia borane. *J. Am. Chem. Soc.* **132**, 1468–1469 (2010).
33. Lin, B. et al. Enhanced ammonia synthesis activity of ceria-supported ruthenium catalysts induced by CO activation. *ACS Catal.* **11**, 1331–1339 (2021).
34. Blochl, P. E., Jepsen, O. & Andersen, O. K. Improved tetrahedron method for Brillouin-zone integrations. *Phys. Rev. B* **49**, 16223–16233 (1994).
35. Kresse, G. & Hafner, J. Ab initio molecular dynamics for liquid metals. *Phys. Rev. B* **47**, 558–561 (1993).
36. Perdew, J. P. et al. Atoms, molecules, solids, and surfaces: applications of the generalized gradient approximation for exchange and correlation. *Phys. Rev. B* **46**, 6671–6687 (1992).
37. Kresse, G. & Joubert, D. From ultrasoft pseudopotentials to the projector augmented-wave method. *Phys. Rev. B* **59**, 1758–1775 (1999).
38. Zhang, D. W., Han, Z. K., Murgida, G. E., Ganduglia-Pirovano, M. V. & Gao, Y. Oxygen-vacancy dynamics and entanglement with polaron hopping at the reduced CeO_2(111) surface. *Phys. Rev. Lett.* **122**, 6 (2019).
39. Chen, H. Z., Zhang, Y. Y., Gong, X. G. & Xiang, H. J. Predicting new TiO_2 phases with low band gaps by a multiobjective global optimization approach. *J. Phys. Chem. C* **118**, 2333–2337 (2014).
40. Zhang, Y. Y., Gao, W. G., Chen, S. Y., Xiang, H. J. & Gong, X. G. Inverse design of materials by multi-objective differential evolution. *Comp. Mater. Sci.* **98**, 51–55 (2015).

Acknowledgements

We acknowledge the financial support of the National Natural Science Foundation of China (52025011, 92045301, 52171019, 52473242, and 52422311), National Key Research and Development Program (2022YFA1505500), the Zhejiang Provincial Natural Science Foundation of China (LR23B030004), the Leading Innovative and Entrepreneur Team Introduction Program of Zhejiang (2023R01007), and the Fundamental Research Funds for the Central Universities.

Author contributions

Y.W. and Y.J. conceived and supervised this study. Z.K.H. supervised the DFT calculations. S.Y.C. performed the in situ TEM observations, data analysis, and drafted the manuscript. K.Z. performed the DFT calculations and contributed to interpreting the results. Y.H.C. and C.Z. helped with the experiments and supported figure making. B.S. helped with DFT calculations. W.T.Y., H.S.Y., and Z.Z. participated in data analysis and revised the manuscript. All the authors commented on the manuscript and have given approval to the final version of the manuscript.

Competing interests

The authors declare no competing interests.

Additional information

Supplementary information The online version contains supplementary material available at https://doi.org/10.1038/s41467-025-60151-3.

Correspondence and requests for materials should be addressed to Zhong-Kang Han, Ying Jiang or Yong Wang.

Peer review information *Nature Communications* thanks the anonymous reviewers for their contribution to the peer review of this work. A peer review file is available.